Immobilization of Orange Carotenoid Protein on mesoporous silica SBA-15 for the development of photoactivable nanodevices

Silvia Leccese, Thomas Onfroy, Adjélé Wilson, Diana Kirilovsky, Sandra Casale, Saremblé Guira, Mohamed Selmane, Claude Jolivalt, Alberto Mezzetti

Immobilization of Orange Carotenoid Protein on mesoporous silica SBA-15 for the development of photoactivable nanodevices

Silvia Leccese[1], Thomas Onfroy[1], Adjélé Wilson[2], Diana Kirilovsky[2], Sandra Casale[1], Saremblé Guira[1], Mohamed Selmane[3], Claude Jolivalt[1*] and Alberto Mezzetti[1*]

(1) Sorbonne Université, CNRS, Laboratoire de Réactivité de Surface, LRS, 4 place Jussieu, 75005 Paris, France

(2) Université Paris-Saclay, CEA, CNRS, Institute for Integrative Biology of the Cell (I2BC), 91198 Gif sur Yvette, France

(3) Sorbonne Université, CNRS, Laboratoire de Chimie de la Matière Condensée de Paris, LCMCP, 4 place Jussieu, 75005 Paris, France

Silvia LECCESE : silvia.leccese@sorbonne-universite.fr
Thomas ONFROY : thomas.onfroy@upmc.fr
Adjélé WILSON : adjele.wilson@cea.fr
Diana KIRILOVSKY : diana.kirilovsky@cea.fr
Sandra CASALE: sandra.casale@upmc.fr
Saremblé GUIRA : saremble.guira@sorbonne-universite.fr
Mohamed SELMANE : mohamed.selmane@sorbonne-universite.fr

(*) Corresponding authors:
Claude Jolivalt : Tel : 33+144276013; claude.jolivalt@ sorbonne-universite.fr
And
Alberto Mezzetti : Tel : 33+144274974 alberto.mezzetti@sorbonne-universite.fr

Abbreviations[1]

[1] Abbreviations

OCP = Orange Carotenoid Protein
ECN = Echinenone
CAN = Canthaxanthin
NTD = N-terminal domain
CTD = C-terminal domain
SBA = Santa Barbara Amorphous

Abstract

The photoactive Orange Carotenoid Protein (OCP) is a protein involved in photo-protective responses in cyanobacteria. It induces the thermal dissipation of excess solar energy counteracting oxidative stress and photodamage. OCP consists of two structural domains sharing a non-covalently linked carotenoid as a cofactor. Blue light induces photoactivation of OCP and its colour changes from orange to red. In this work we have immobilized OCP on different kinds of raw and surface-functionalized SBA-15 mesoporous silica nanoparticles and structurally characterized the systems. SBA-15 matrices have demonstrated to be suitable supports for OCP, whose immobilization is strongly enhanced by the pre-photoactivation of the protein. OCP remains photoactive inside the mesoporous silica matrix, thereby producing photochromic nanoparticles. Under appropriate conditions OCP can also be released from SBA-15 nanoparticles. This work is a first step to understand the influence of matrix constraints and confinement on OCP photocycle. Furthermore, this study demonstrates that the OCP@SBA-15 system can be used as a photochromic material and as a possible optical device for nanoscale applications. Finally, this work is a first step towards the development of caroteno-protein and carotenoid release-strategies from silica matrix to be applied in the field of antioxidant drug delivery.

Keywords

Orange Carotenoid Protein, SBA-15, protein immobilization, photochromic nanoparticles, drug delivery

1. Introduction

Structured mesoporous materials have always been considered of great interest for their advantageous properties such as highly reproducible structure with narrow pore size distribution, wide pore diameter range, high surface area and pore volume [1,2]. These structural and textural peculiarities let Ordered Mesoporous Materials (OMMs) be considered for applications involving proteins and enzymes because they promise to be solid supports able to preserve the stability of these biological systems [3]. The immobilization of proteins together with the stabilization of their native conformation after the interaction with mesostructured surfaces is increasingly considered for a wide range of nanobiotechnological applications such as biocatalysis, sensoring, nanomedicine and tissue engineering [3,4]. These applications depend on protein adsorption, whose uptake capacity is shown to be strongly correlated with the protein size, mesopore diameter and pore volume [1].

This study focuses the attention on Orange Carotenoid Protein (OCP), a water-soluble protein involved in photoprotection of cyanobacteria [5,6] which, as other photosynthetic organisms, have developed protective mechanisms to prevent oxidative damage under excessive light exposure. In OCP a keto-carotenoid (3-hydroxyechinenone, echinenone (ECN) or canthaxanthin (CAN)) is embedded but non-covalently linked between two structural domains of OCP (called N-terminal domain – NTD and C-terminal domain – CTD) and is therefore only sparingly solvent accessible (Figure 1). Absorption of a blue photon (450–500 nm) triggers large-scale structural modifications of OCP involving the whole protein backbone, so that OCP changes from the resting, dark-adapted orange state (OCP^O), to its so-called active red state (OCP^R). Only OCP^R is able to induce the

quenching of absorbed energy, preventing photo-damage of the cyanobacterial photosynthetic apparatus [5].

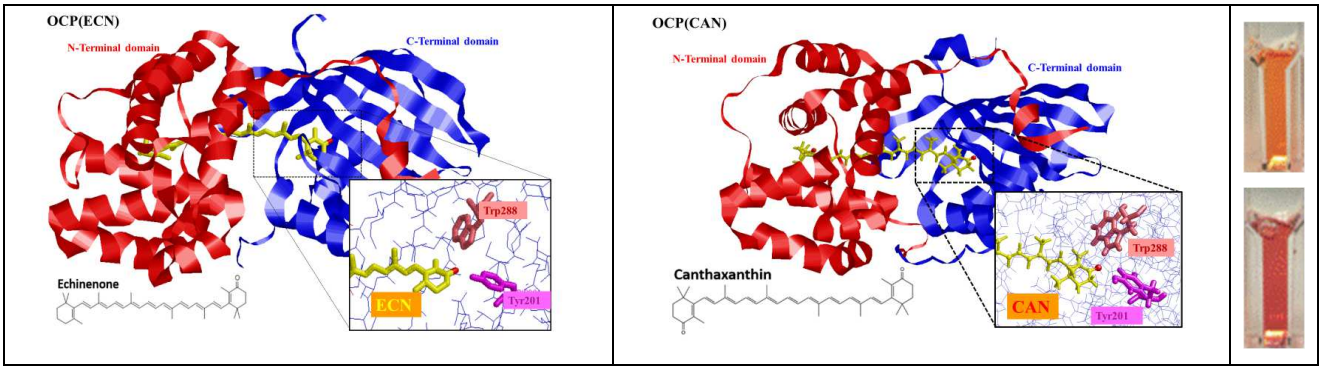

Figure 1. (Left) Crystal structure of OCP binding Echinenone from cyanobacteria Synechocystis PCC 6803 (PDB 3mg1 [7]). (Middle) Crystal structure of OCP binding Canthaxanthin from cyanobacteria Synechocystis PCC 6803 (PDB 4xb5 [8]). ECN and CAN are depicted in yellow in the 3D view, with oxygen atoms in red. In the bottom, left corner of each picture there is the chemical structure of ECN and CAN; in the bottom, right corner there is a zoom-in on interactions between the carbonyl group of carotenoids and amino acids Tyr201 and Trp288 belonging to the C-terminal domain. (Right) OCP in solution before photoactivation (OCP^O) (top) and OCP in solution after photoactivation (OCP^R) (bottom).

Carotenoids thus play a key role in the mechanism of photoprotection of cyanobacteria. More generally, these hydrophobic chromophore molecules derived from the isoprenoid metabolism are responsible for light harvesting and photoprotective reactions [9] as well as defense mechanisms against oxidative stress, not only in photosynthetic organisms, but also in animals [10–12]. Because OCP is a water-soluble protein, it could be a suitable delivery vector of carotenoids. Indeed, recently an OCP-related cyanobacterial caroteno-protein named AnaCTDH has been used for carotenoid delivery to membranes of mammalian cells [13]. One suitable option to protect OCP (e.g., from enzymatic degradation of harsh pH conditions) and to modulate the carotenoid delivery conditions would be to encapsulate OCP into a mesoporous inorganic material. It should be mentioned that beside its use as antioxidant, several applications of OCP have been recently proposed, ranging from its use as optical switch and photoprotective element [14] to regulator of fluorescence in biosensors [15,16]. Furthermore, not only different kind of OCP (with different properties) have been identified [17], but also several homologs of NTD and CTD domains exist [5], so that artificial OCP-like protein can be constructed [18]. This, along with specific genetic engineering techniques [16,19] can make it possible to develop photoactivable and photochromic caroteno-proteins with tailored properties (for instance OCP-like structures which upon light activation can form a separate and smaller NTD-like carotenoid-containing proteins [20]).

Among the numerous mesoporous materials described in the literature for their ability to immobilize proteins [21], SBA-15 (Santa Barbara Amorphous) was chosen as an inorganic support for OCP. This nanoporous material, synthesized for the first time in 1998 [22], is an ordered mesoporous silica material with regular, hexagonal pores whose size can be tuned from 2 and 50 nm wide and from 200 nm up to a few µm long. Smaller micropores connect mesopores with each other [23]. It is characterized by highly uniform porosity, good mechanical stiffness, thermal stability, a high pore volume and a large specific surface area. These materials have attracted much attention as hosts for immobilization of enzymes as well as delivery systems [21]. The structural parameters of SBA-15, such as the diameter of pores and micro-porosity can be modified by tuning parameters of its synthesis [24]. Besides to the possibility to adjust the size of the pores, the ability to modify the surface properties of these materials to match the targeted biomolecules can provide higher protein

immobilization capacity [21,25]. Such an enhancement of apparent solubility of compound of pharmaceutical interest in order to improve their bioavailability and their pharmacokinetic properties is emerging as an area where mesoporous materials can provide valuable benefit. Numerous biomedical applications in small molecules or protein delivery, including drug targeting strategies have consequently gained much attention [26,27]. Others advantages of the use of non-toxic SBA-15 in the immunology field were that it does not cause any damage in the application area of injection while being an efficient adjuvant [28].

The aim of this study is thus to immobilize OCP on a mesoporous SBA-15 to study the influence of structural and textural features of SBA-15 on the chemical properties of OCP and to assess the photochromic behavior of the immobilized protein and its stability in time. SBA-15 with two different pore sizes, namely SBA-15-80 and SBA-15-120, is used to assess a possible effect of the confinement of OCP insides the pores in terms of protein loading but also influence of surface interactions on protein structure and dynamics. To modulate the interaction between SBA-15 and the protein, the material has been functionalized with covalently bound aminopropyl groups (SBA-15-NH_2) which are likely to influence the electrostatic interactions between the solid and the protein, and consequently the OCP immobilization yield by adsorption. In addition, a modified surface may also interfere with the photoactivation process of the protein.

2. Experimental section

2.1. Expression of *Synechocystis*-OCP in *E. coli*.

Recombinant OCP(ECN) and OCP(CAN) from *Synechocystis sp.* were produced in *E. coli* according to the protocol reported by Bourcier de Carbon et al. [29].

2.2. Synthesis of SBA-15

SBA-15 was synthesized as reported in the literature using a triblock copolymer, Pluronic P123 ($(EO)_{20}(PO)_{70}(EO)_{20}$ from Aldrich) as a structure directing agent [22]. In a typical synthesis 8.02 g of P123 were mixed under stirring (750 rpm) with 280 mL of 0.1 mol/L HCl for 2 hours at 40°C until complete dissolution of P123 and the creation of a mesostructured phase of micelles. Then 16.80 g of tetraethyl-orthosilicate (TEOS; Aldrich; 98%) as silica precursor was added drop by drop to the solution under slower stirring (ca. 500 rpm). The resulting suspension has been let under stirring for 24 hours to allow the formation of a mesostructured silica sol-gel. The sol-gel suspension has then been transferred into a 1 L glass bottle and hydrothermally treated for 24 hours at 80°C or 120°C. Finally, the obtained solid was filtrated and thoroughly washed with distilled water (approx. 4 L) to remove the P123 polymer. The resulting powder has been dried at 80°C or 120°C overnight and calcined at 550°C (heating ramp: 0.4°C min^{-1}) for 6 hours under air to remove the template. Finally, around 4 g of SBA-15 material was obtained.

2.3. Surface functionalization: SBA-15-NH_2

Prior to the functionalization, 1g of SBA-15 has been placed in a reactor and activated at 350°C (heating ramp: 5°C min^{-1}) for 3 hours under 50 mL min^{-1} air flow (Air Liquide). Silica has been then transferred into a dried balloon equipped with a septum. 50 mL of commercial anhydrous toluene (VWR, 99.9%) have been added to silica. The balloon has been then flushed with argon for few

minutes and then let for 5 minutes in ultrasonic bath to get a perfect silica suspension. The balloon has been finally connected to a refrigerator and placed under argon flow. To start the functionalization reaction, 1 mL of 3-aminopropyltriethoxysilane (ATPES; Aldrich; 99%) has been added to the suspension drop by drop. Then, Argon flow stopped, the suspension has been stirred for 1 hour at room temperature and then for 24 hours refluxing (120°C). Finally, the mixture has been filtrated on Büchner and filter paper and washed with 30 mL of anhydrous toluene (VWR, 99.9%), 30 mL of acetonitrile (VWR; HPLC grade) and 30 mL of absolute ethanol (Aldrich; 99.9%). The resulting solid has been dried at 60°C over-night. The excess of APTES has been extracted with Soxhlet apparatus, introducing 50 mL of CH_2Cl_2 (Carlo Erba Reagents; 99.9%) in a balloon and refluxing the system at 45°C for 24 hours. Finally, the functionalized silica has been dried at 60°C over-night.

2.4. Immobilization of OCP on SBA-15

Typically, 1 mL of a 0.2 mg/mL OCP solution in water was mixed with 10 mg silica powder. The mixture (pH 8.5) was incubated under gentle stirring for 4 hours (except for time course experiments) at room temperature in the dark, to avoid the photo-activation of the protein, then overnight at 4°C. The initial concentration of OCP or the stirring duration of the suspension varied for the adsorption isotherm and kinetics experiments. IE (immobilization efficiency) of OCP has been calculated by measuring the supernatant absorbance Abs_{supnat} at 474 nm and subtracting this value from the initial OCP absorbance:

$$IE\ \% = \frac{Abs_{OCP} - Abs_{supnat}}{Abs_{OCP}} \times 100$$

2.5. Leaching extent of OCP(CAN) from SBA-15-80 and SBA-15-80-NH_2

To study the release of OCP from silica matrices, two different procedures were used. Firstly, the ionic strength effect was tested: OCP (1 mg/mL) immobilized on 10 mg of silica was suspended in 5 mL of NaCl solution 1 M, the mixture (pH 6.9 for SBA-15-80 sample and pH 8.4 for SBA-15-80-NH_2) was gently stirred at room temperature in the dark. Leaching extent has been calculated by measuring the supernatant absorbance at 474 nm each 24h, for 1 week. Furthermore, pH effect was tested: OCP (1 mg/mL) immobilized on 10 mg of SBA-15-80-NH_2 was suspended in 5 mL of Acetic acid/Acetate buffer 50 mM (pH 4.3) to have either OCP or SBA-15-NH_2 positively charged; the mixture (pH 4.2) was gently stirred at room temperature in the dark. In parallel, OCP immobilized on 10 mg of SBA-15-80 was suspended in 5 mL of Phosphate buffer 50 mM (pH 7.3) to have either OCP or SBA-15 negatively charged; the mixture (pH 6.9) was gently stirred at room temperature in the dark. Leaching extent has been calculated by measuring the supernatant absorbance at 474 nm each 24h, for 1 week.

2.6. UV-visible spectroscopy in liquid and solid phase

Absorption spectra of solids were recorded on a Varian 2300 UV Vis spectrophotometer equipped with an integrating sphere between 350 and 750 nm with a resolution of 1 nm and an acquisition time of 0.1 s per point. Absorption spectra in liquid phase were recorded on Biochrom Libra S60 spectrophotometer, between 350 and 750 nm with a resolution of 0.5 nm and an acquisition time of 0.1 s per point.

2.7. Small angle - XRD analysis

The X-ray diffraction has been used to identify crystalline structure of the pure and functionalized SBA-15. Analysis have been performed from 0.4° to 5° (2θ) in steps of 0.01° with a count time of

90 s for each point. The Cu K_α (λ = 1.5418 Å) was the source of X-ray radiation. The XRD analysis have been performed using a Shimadzu XRD-6000 (Japan) X-ray diffractometer.

2.8. Electronic microscopy

The morphology of the solids was investigated with a high-resolution SEM-FEG Hitachi SU-70 operating at an acceleration voltage of 1.0 kV and at a working distance of 3 mm. Transmission electron microscopy (HRTEM) was performed on a JEOL JEM 1011 (W) microscope operating at 100 kV and equipped with an ORIUS Gatan Camera. For TEM observations, the sample powders were deposited on a 3 mm copper grid coated with an amorphous carbon film. The samples were prepared by dispersing in pure alcohol using ultrasonic cleaner and putting a drop of this suspension on carbon films on copper grids.

2.9. Thermogravimetric analysis (TGA)

The TGA has been used to characterize the weight loss due to absorption/desorption of OCP but also to estimate the amount of aminopropyl group grafted during the SBA-15 functionalization. TGA analysis have been performed on STD Q600 thermobalance (TA Instrument). The weight loss has been measured while heating from 30 to 700°C (heating rate 5°C min^{-1}) under air flow (100 mL min^{-1}).

2.10. Nitrogen adsorption / desorption isotherms

The specific surface area, pore size distribution and total pore volume of SBA-15 and SBA-15-NH_2 before and after adsorption of OCP were determined by recording nitrogen adsorption isotherms. Prior to the experiment, a degassing pre-treatment has been applied to the samples: empty SBA-15 was dehydrated at 120°C overnight while SBA-15-NH_2 and OCP loaded SBA-15 were dehydrated at 40°C for 30 minutes then at 60°C for other 30 minutes under vacuum. Such low temperature pre-treatment has been chosen to prevent thermal degradation of the grafted aminopropyl group or/and adsorbed protein. As a control, the same degassing pre-treatment at low temperature was used with OCP immobilized on SBA-15 and on SBA-15 treated with water but in absence of OCP, to allow the comparison between samples with or without protein. Indeed, pre-treatment at low temperature does not completely remove water from micropores and this could affect the comparison. Nitrogen adsorption isotherms at -196°C were measured on BELSORP max apparatus. The specific surface area was obtained from adsorption values by using the Brunauer – Emmett – Teller equation at six relative pressures (P/P_0) ranging from 0.04 to 0.25. The total pore volume was determined from the amount of N_2 adsorbed at P/P_0= 0.975. The diameter of mesopores was obtained from the pore size distribution calculated using the Barrett – Joyner – Halenda (BJH) equation applied to the desorption branch of the isotherm.

3. Results and discussion

3.1. Structural and textural characterization of SBA-15 and SBA-15-NH_2

Two SBA-15 type solids were synthesized by tuning the aging temperature at 80 and 120°C. Consequently, these materials are denoted as SBA-15-80 and SBA-15-120, respectively, hereafter in the text. Their structural and textural properties are summarized in Table 1. The XRD pattern (Figure 2.a) confirmed that SBA-15 with well-ordered 2D hexagonal pores was obtained in both cases: for SBA-15-80 a single high-intensity peak at 2Θ = 0.89° and two additional smaller peaks, at 2Θ =

1.53° and 1.76° can be attributed to (100), (110) and (200) diffraction planes of a hexagonal lattice of p6mm symmetry. For SBA-15-120, the peaks are slightly shifted to 2Θ = 0.97°; 1.60° and 1.84° and an increase of the SBA-15 cell parameter (a_0) was observed (Table 1). Such an influence of aging temperature on crystal parameters was already reported in the literature[30–33] and interpreted as a result of the shrinking of the SBA-15 structure during the calcination step after an aging step at lower temperature[32]. The length of the hexagonal cell unit a_0 was calculated using the XRD (100) interplanar spacing value, namely d_{100}. A large pore wall thickness W larger than 4 nm, according to the formula $W = a_0 - D_{BJH}$ is thus observed for both solids (Table 1).

To complete XRD analysis, SBA-15 type materials have been studied by Scanning Electron Microscopy (SEM) and Transmission Electron Microscopy (TEM). According to the SEM image (Figure 2.b), SBA-15 particles present a worm shape morphology with a width of about 0.2 to 0.4 µm and a length of 1 to 2 µm. In addition, TEM image of SBA-15 (Figure 2.d) clearly shows a well-ordered material with perfectly aligned silica walls and pores.

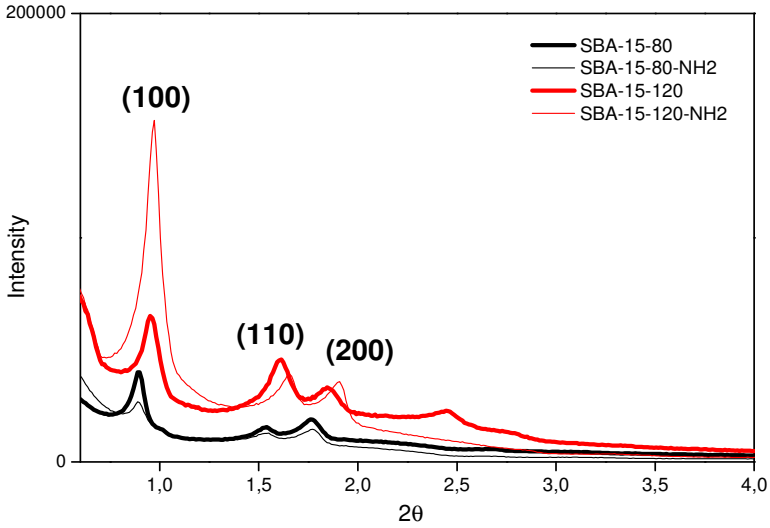

(a)

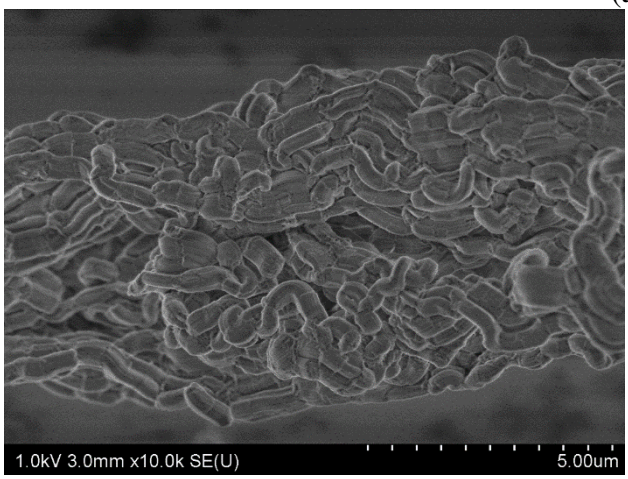

(b)

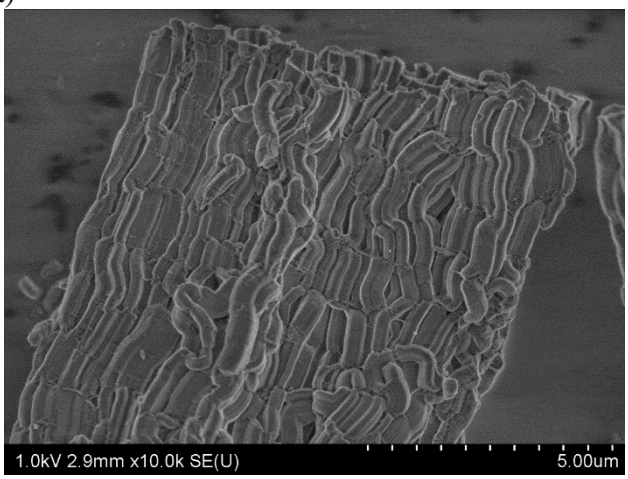

(c)

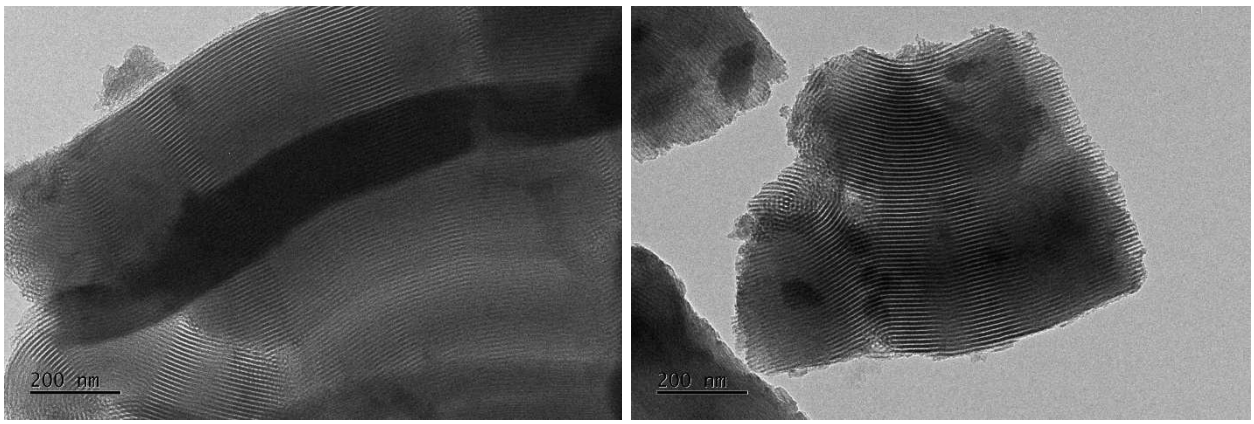

(d) (e)

Figure 2: (a) XRD powder pattern of SBA-15 and SBA-15-NH_2 materials prepared at 80°C or 120°C as aging temperature; (b) and (c) SEM images of SBA-15-80 and SBA-15-80-NH_2; (d) and (e) TEM images of SBA-15-80 and SBA-15-80-NH_2.

The nitrogen adsorption-desorption isotherms at 77 K (Figure 3) are of type IV according to the IUPAC classification and exhibited a H1-type hysteresis loop with parallel adsorption and desorption branches which is typical of mesoporous materials with cylindrical channels in a hexagonal arrangement [34,35]. For relative pressure (P/P_0) in the range from 0.7 to 0.8, isotherms exhibit a steep slope characteristic of capillary condensation of nitrogen within uniform mesopores, where the P/P_0 position of the inflection point is correlated to the diameter of the mesopores.

Depending on the aging temperature during the synthesis, materials pore size increased from 5.8 nm to 7.7 nm when aging at 80 and 120°C respectively (the textural properties for SBA-15 samples are summarized in Table 1). The effect of increasing the aging temperature thus led to an increase of the pore diameter, as extensively reported in the literature [22,34,36,37]. The rise of temperature during hydrothermal synthesis indeed induces an increase of the aggregation number of the surfactant (P123), and consequently of the volume of the formed micelles, leading to an increase of pore size [1]. In their pioneer work dealing with SBA-15 synthesis, Zhao *et al* obtained a solid with an 8.9 nm mean pore diameter after aging at 100°C for 48 hours while very similar TEOS hydrolysis and gel ripening conditions were used in the present work. A shorter aging duration, i.e., 24 hours used in the present work could explain the difference in the pore diameter. The BET surface areas of SBA-15-80 and SBA-15-120 were found to be 759 and 576 m^2/g, respectively, in good agreement with the literature [2,36,38–42]. Such an inverse correlation between the pore size and the material surface is indeed as a consequence of the cylindrical shape of the mesopores [2].

Solid Name	Aging temperature (°C)	d_{100} (nm)	a_0 (nm)	D_{BJH} (nm)	SA_{BET} (m^2/g)	PV (cm^3/g)
SBA-15-80	80	9.92	11.5	5.8	759	0.90
SBA-15-80-NH_2	80	9.92	11.5	5.4	344	0.52
SBA-15-120	120	10.51	12.1	7.7	576	1.22
SBA-15-120-NH_2	120	10.64	12.3	6.7	312	0.69

Table 1: Properties of SBA-15 used for OPC adsorption studies. Where d_{100} is the interplanar spacing; a_0 the unit cell parameter ($a_0 = 2\times d_{100}/\sqrt{3}$); SA_{BET} is the BET surface area; PV the pore volume calculated at $P/P_0 = 0.975$

In order to modify the physico-chemical properties of the solid surface to influence the subsequent protein immobilization efficiency, which is the main objective of this study, SBA-15 was grafted with

3-aminopropyltriethoxysilane (APTES) by a post-synthesis modification of the SBA-15 silanol groups. XRD pattern of SBA-15-NH_2 was very similar to the one of SBA-15 prior to its functionalization, thus evidencing that the functionalization of the SBA-15 surface with –NH_2 groups did not affect the crystalline structure of the mesoporous material (Figure 2.a). This is confirmed by SEM and TEM images. Indeed, the functionalized SBA-15 particles (Figure 2.c) present the same size and morphology as the bare SBA-15 (Figure 2.b). In addition, comparison of TEM images of bare SBA-15 (Figure 2.d) and SBA-15-NH_2 (Figure 2.e) clearly evidenced that the functionalization step does not induce any modification of the meso-structuration of silica support. Furthermore, the nitrogen sorption isotherms of organo-functionalized SBA-15-NH_2 samples (Figure 3.a-b) show the same type IV isotherms and type H1 hysteresis loop as the ungrafted SBA-15 ones. Functionalization unequivocally results in reduced pore sizes compared to the un-functionalized materials, as indicated by the pore size distribution curves (Figure 3.c-d). The mean pore size varies from 7.7 to 6.7 for SBA-15-120-NH_2, and from 5.8 to 5.4 form SBA-15-80, in line with literature results [43]. The decrease of the pore diameter is likely to be a consequence of the presence of the space filling grafted 3-aminopropyl groups, which is corroborated by the decrease of the total pore volume after APTES grafting (see Table 1) [40,44]. The quantification of the number of organic moieties grafted on SBA-15 was performed by thermogravimetric analysis (TGA). For SBA-15-80 one major weight loss event (around 10 %) was observed in the temperature range between 300 and 700°C (Figure 3.e) which can be ascribed to the loss of aminopropyl groups [41,42] and allowed to estimate the density of NH_2 groups grafted on SBA-15-80-NH_2 to 1.72 mmol/g (or 1.36 –NH_2 groups/nm^2). For SBA-15-120 one major weight loss (around 18 %) event was observed in the temperature range between 300 and 700°C (Figure 3.f) which allowed estimating the density of NH_2 groups grafted on SBA-15-120-NH_2 to 3.1 mmol/g (or 3.2 –NH_2 groups/nm^2).

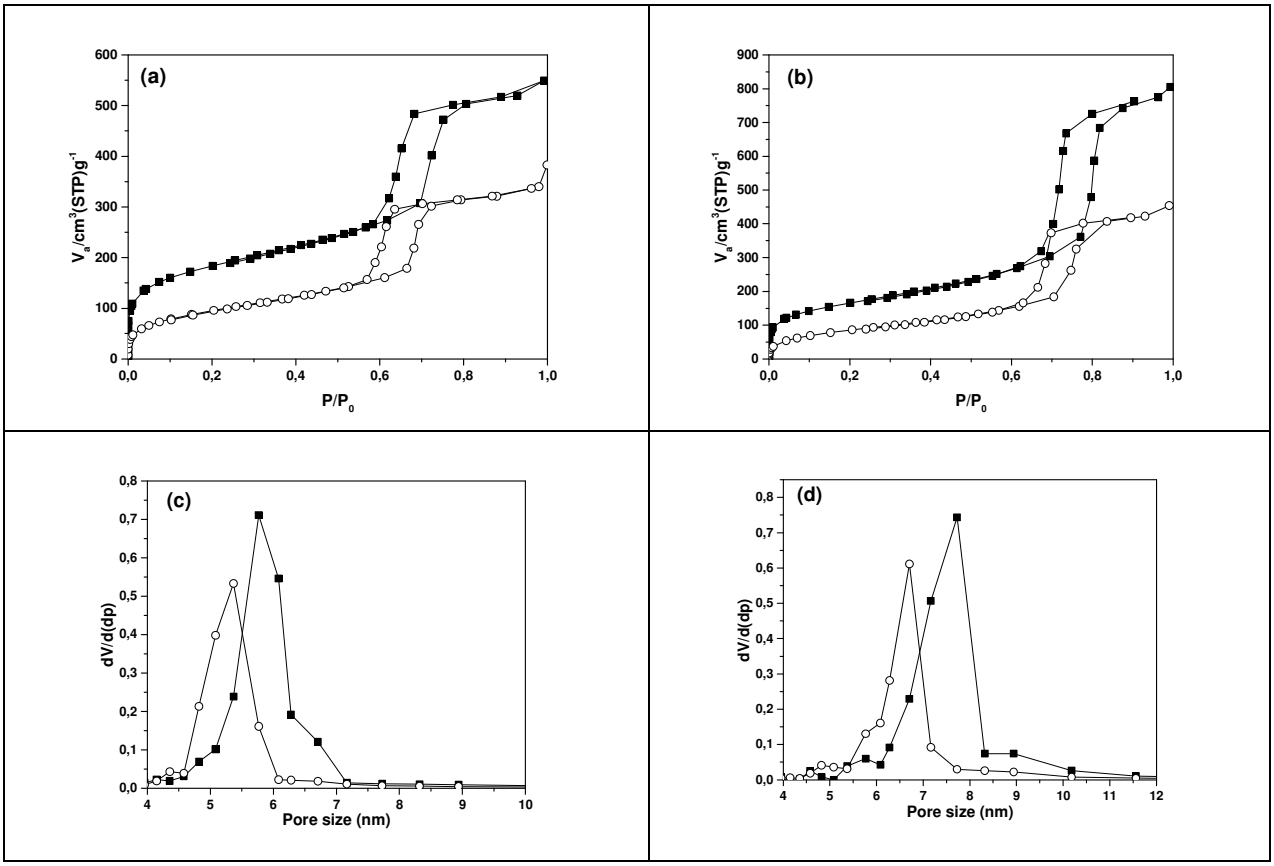

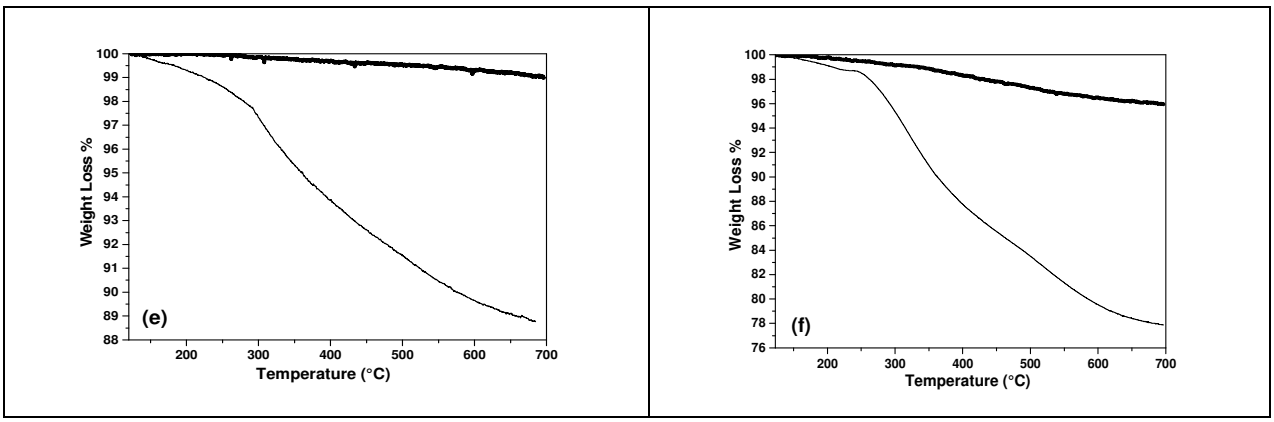

Figure 3. (a) N_2 adsorption isotherm of the bare SBA-15-80 (full square) and the functionalized SBA-15-NH_2 (open circle); (b) N_2 adsorption isotherm of the bare SBA-15-120 (full square) and the functionalized SBA-15-NH_2 (open circle). (c) Pore size distribution calculated on SBA-15-80 (full square) and functionalized SBA-15-NH_2 (open circle); (d) Pore size distribution calculated on SBA-15-120 (full square) and functionalized SBA-15-NH_2 (open circle). (e) TGA analysis of SBA-15-80 and (f) SBA-15-120 before (thick) and after (thin) –NH_2 functionalization.

3.2. Immobilization of OCP(ECN) or OCP(CAN) in mesoporous SBA-15

OCP was adsorbed on four different mesoporous silica matrices: SBA-15-80, SBA-15-120 and their derivatives functionalized with amino groups. Two OCPs were studied, which contained two different carotenoids, namely echinenone (ECN) and canthaxanthin (CAN). Only these ketocarotenoproteins (in addition to 3-hydroxyechinenone, 3h-ECN) make OCP photoactive.

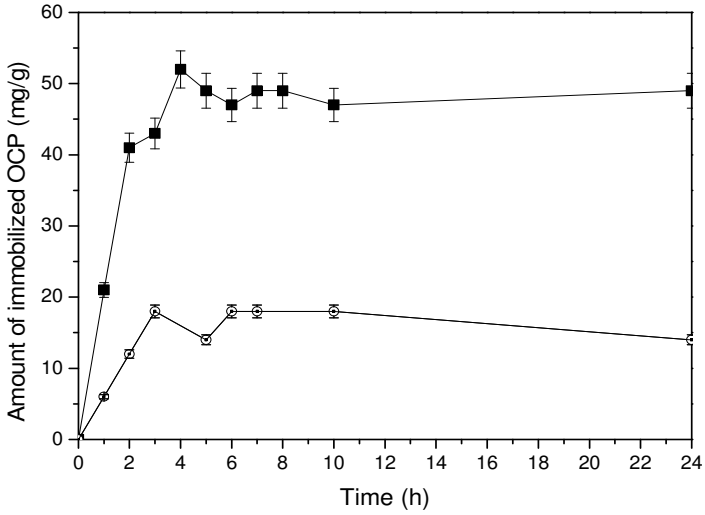

Figure 4: OCP(CAN) adsorption on SBA-15-80 (full square) and SBA-15-80-NH_2 (open circle) followed-up in time. Initial OCP(CAN) concentration 2 mg/mL (50µM).

OCP was immobilized on SBA-15 by adsorption on the solid support. The kinetics of the adsorption process was studied with OCP(CAN) and showed that the amount of immobilized OCP on both SBA-15-80 and SBA-15-80-NH_2 silica materials increased with time from 0 to 4 hours (Figure 4). Then, a plateau was reached for SBA-15-80 as well as for SBA-15-80-NH_2 although a slight decrease of the protein uptake was observed for the latter solid after a 24h long experiment. However, it could be concluded that the equilibrium was almost reached after around 4 hours for both materials.

The loading efficiencies of OCP(CAN) and OCP(ECN) are shown in Figure 5 and Table 2. The OCP adsorption behavior on SBA-15-80 as a function of the initial protein concentration (Figure 5) follows a typical isotherm adsorption profile on solids, with an increase of the amount of immobilized protein when increasing the initial protein concentration. At the maximum tested initial OCP(CAN) concentration, namely 2 mg/mL, the protein loading reached 52 mg/g of solid. As an attempt to provide an alternative measurement of the protein uptake, thermogravimetric analysis has been also performed, showing a weight loss of 88 mg/g between 120 and 700 °C (see Figure S1 in the supporting information part). The overestimation of the protein loading from thermogravimetry analysis compared to absorbance measurements of the solution could arise from the presence of water bound to the protein and released from the support at higher temperatures than free water, thus increasing the overall weight loss. Thermogravimetric analysis was consequently not further used for OCP uptake quantification. In the whole range of protein initial concentration tested, as the slope of the adsorption isotherm remains positive, it is expected that maximum loading capacity of SBA-15-80 was not reached, in line with results reported in the literature for several other proteins such as lysozyme, bovine serum albumin, glucose oxidase, cytochrome c or myoglobin whose loading capacity was shown to reach several hundreds of mg/g of SBA-15 or SBA-15-type mesoporous silicas [1,2,36,38,40,43,45,46].

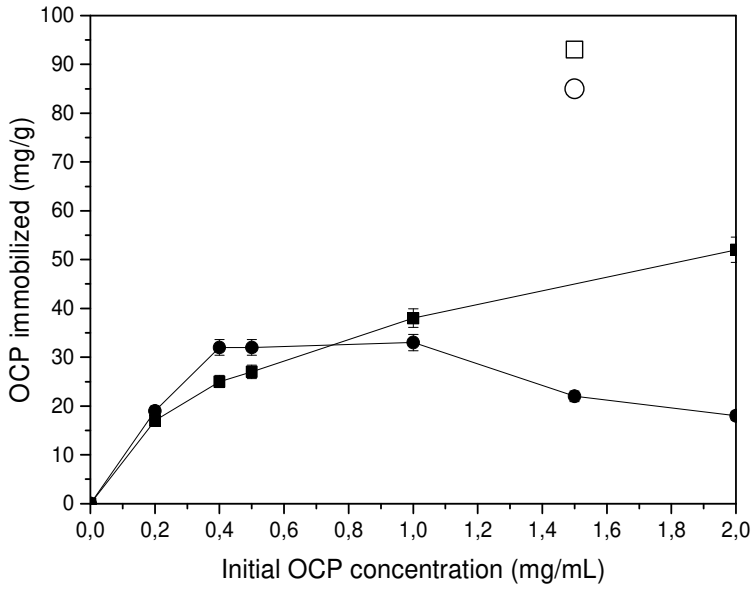

Figure 5: OCP(CAN) adsorption isotherms on SBA-15-80 (solid square) and SBA-15-80-NH_2 (solid circle). OCP(CAN) adsorption isotherms on SBA-15-80 under blue light LED (open square) and SBA-15-80-NH_2 (open circle).

Size of the protein relative to the one of the SBA-15 pores as well as electrostatic interactions with the solid surface being two main parameters governing the adsorption efficiency, it is worth taking account of the latter parameters with the ones of OCP for a more accurate comparison. Indeed, lysozyme (molecular weight 15 kDa) was found to adsorb in larger amount on SBA-15 (450 mg/g of solid) than bovine serum albumin (molecular weight 66.5 kDa) whose maximum uptake capacity on the same support was limited to 58 mg/g [47]. OCP has a molecular weight around 35 kDa, so that its maximum binding capacity on SBA-15-80 is expected to be lower than the one of lysozyme, a smaller protein, but higher than the one of bovine serum albumin, a larger protein. The large SBA-15-80 uptake capacity of lysozyme reported in the work of Sang et al. [47] also originates in favor-

able electrostatic interactions between the silica surface and the protein since the pH of the solution was chosen to be equal to the isoelectric point of lysozyme (pH 11) in order to minimize repulsion between protein molecules and consequently favors a close packing of the protein inside the mesopores [1,43,48,49]. In the present work, the pH of the protein solution was around 8.5 (storage pH of OCP after its purification process). In such conditions, OCP, whose isoelectric point (pI) value is around 5.4, is negatively charged. The unfavorable interactions with the silica surface, whose zeta potential is negative for pH >2 due to the deprotonation of the silanol groups [39], are thus likely to limit the protein uptake. The amount of absorbed protein varied in these conditions from around 16 mg/g of SBA-15 for OCP(CAN) to 19 mg/g for OCP(ECN). Overall, the obtained protein loading on SBA-15 was suitable for the further photosensitivity analysis, which are the main objectives of the study, even at the lowest OCP initial concentration tested, ie 0.2 mg/mL.

Immobilization Efficiency	**SBA-15-120**	**SBA-15-120-NH_2**	**SBA-15-80**	**SBA-15-80-NH_2**
OCP(ECN)	93%	95%	71.7 ± 2.8 %	84.1 ± 6.5 %
OCP(CAN)	80%	85%	83.0 ± 1.1 %	94.9 ± 5.4 %

Table 2. Immobilization efficiency % of OCP(ECN) and OCP(CAN) in SBA-15120 and SBA-15-80 and the corresponding functionalized SBA-15-NH_2. OCP initial concentration: 0.2 mg/mL. The experimental error has been calculated only on SBA-15-80 samples.

According to Table 2, another parameter that influences OCP(ECN) immobilization efficiency is the pore size of the silica mesoporous materials. Indeed, it was observed that the protein adsorption was favored on SBA-15 with larger pore size, which could result from a better diffusion of OCP inside channels of mean 7.7 nm diameter than inside smaller ones (mean 5.7 nm pore diameter for SBA-15-80), knowing the dimensions of a OCP monomer are around 4*4*7.5 nm [7]. Such a conclusion however does not apply to OCP(CAN), whose dimensions are yet the same as the OCP(ECN) ones and differs from the latter only by the presence of ECN instead of CAN, both carotenoids being buried in the protein pocket, with no influence on the surface electrostatic properties of the protein. Further investigations at higher OCP initial concentration could provide additional information to explain the effect of the pore size upon OCP adsorption.

In order to modulate the electrostatic interactions that govern the adsorption of OCP on the mesoporous solid, SBA-15 was functionalized by grafting of aminopropyl groups. As shown from zeta potential measurements (Fig. SI.2), SBA-15-NH_2 surface remains positive in the pH range between 4 and 8. As OCP isoelectric point is around 5.4, as calculated from its primary sequence (3MG1 pdb file), the protein is overall negatively charged at pH 8.5 where the adsorption process takes place. In such conditions, electrostatic interactions are thus expected to favor OCP adsorption compared to immobilization on bare SBA-15. However, as shown in Table 2, at low OCP initial concentration (0.2 mg/mL), SBA-15-120-NH_2 led to unchanged (within the experimental error) OCP immobilization efficiencies compared to SBA-15-120 while for SBA-15-80, only a slight, although significant, increase of the protein loading was observed from 71.7 ± 2.8 % to 84.1 ± 6.5 % for OCP(ECN) and 83.0 ± 1.1 % to 94.9 ± 5.4 % for OCP(CAN). This latter expected result could thus arise from local favorable electrostatic interactions between the positively charged aminopropyl groups and deprotonated carboxylic groups (pKa around 5) on OCP. Such a favorable effect however was not observed for SBA-15-120-NH_2. One explanation for this behavior could result from the ability of both OCP^O and OCP^R to dimerize at high solution concentration [50,51]. OCP dimers are thus likely to be adsorbed inside the mesoporosity of SBA-15-120, whose pores are large enough to accommo-

date the dimer. However, the dimer surface charge distribution could be modified compared to the monomer one, thus inducing less favorable electrostatic interactions with the silica support. Finally, a lower OCP uptake capacity on SBA-15-80-NH_2 compared to SBA-15-80 was observed for high initial OCP concentrations: 18 and 52 mg/g, respectively for 2 mg/mL OCP initial concentration (Figure 5). A maximum immobilization amount of 33 mg/g was reached on SBA-15-80-NH_2 for 1 mg/mL OCP initial concentration. When the latter was further increased, a decrease of the amount of immobilized OCP was found, opposite to what was observed with SBA-15-80. Such a saturation effect could be related to the support properties: protein/support interactions could be too strong to allow any diffusion of the protein inside the pores, so that OCP is located only at the pores entrance and may block pores upon adsorption hindering further protein uptake [36].

As an additional experiment, adsorption of OCP(CAN) was performed while the protein was illuminated by a blue light LED (λ = 475nm). For both SBA-15-80 and SBA-15-80-NH_2, OCP(CAN) adsorption was substantially enhanced: from 52 to 93 mg/g on SBA-15-80 and from 18 to 85 mg/g on SBA-15-80-NH_2 (Figure 5). Such an improvement of the uptake capacity could result from the conformational modifications of OCP upon activation of the protein by light. These conformational changes are critical for OCP function since OCP^R is able to bind the purified phycobilisomes in vitro, whereas OCP^O does not [52]. The active OCP^R form appears to have a more open conformation and an increased surface exposure of the interface between the N- and C-terminal domains [53]. Dynamic X-ray crystallography (OCP(ECN) and OCP(CAN) from Synechocystis PCC6803) has identified some structural intermediates of OCP photo-conversion process, showing that H-bonds between the ketolated β-ring of carotenoid and both Tyr-201 and Trp-288 are broken, allowing a 12 Å long translocation of the carotenoid towards the N-terminal domain whose α-helices move away from C-terminal domain leading to solvent exposure of both carotenoids β rings [8,53–55]. As a consequence, the conformational changes associated with OCP activation are therefore significant with an OCP^R molecule with a more elongated shape compared to OCP^O [54]. Furthermore, it was shown that while at high concentration OCP^O dimerizes in a globular shape, OCP^R forms dimers with a more elongated shape [56]. Such significant structural modifications of OCP^O upon illumination which lead to reduced dimensions of OCP, could therefore explain the enhanced amount of immobilized OCP since the OCP^R, having a reduced steric hindrance, could more easily diffuse into the mesopores.

An argument corroborating the hypothesis of a possible adsorption of OCP inside the SBA-15 porosity is that OCP adsorption led to the modification of the meso-porous volume and pore size distribution of the material, determined from the desorption branch of the isotherm using the BJH model, as depicted in Figure 6. N_2 physisorption analysis was conducted on samples with the maximum loading of OCP(CAN) on bare and organo-functionalized SBA-15-80. As a control, the pore size distribution was calculated for an SBA-15 sample whose nitrogen sorption pretreatment was the same as the one performed for OCP loaded on solid, i.e. at 30°C for 36h to avoid any OCP degradation. The meso-porous volume of SBA-15-80 was reduced from 0.64 cm^3/g to 0.57 cm^3/g after OCP loading (93 mg/g), while the meso-porous volume of SBA-15-80-NH_2 from 0.45 cm^3/g to 0.27 cm^3/g after OCP loading (85 mg/g). No reduction of pore size distribution is shown for SBA-15-80 after OCP loading. However, for SBA-15-80-NH_2, the pore size distribution was significantly shifted towards lower pore sizes. Instead of the maximal pore size at 5.4 nm before OCP adsorption, two maxima were observed for SBA-15-80-NH_2 after OCP immobilization at around 4.8 nm and 4 nm. Such a smaller pore size could result from the adsorption of OCP inside the mesoporosity of SBA-

15-80-NH_2. The combination of these two results, notably the reduction of meso-porous volume and pore size distribution, suggests the idea that nanopores are partially occupied by OCP molecules (the volume occupied by 20 mg of OCP molecules/g of SBA-15 is around 0.02 cm^3/g if considering its shape comparable to an ellipsoid) even if OCP could lock pores entrance preventing further loading.

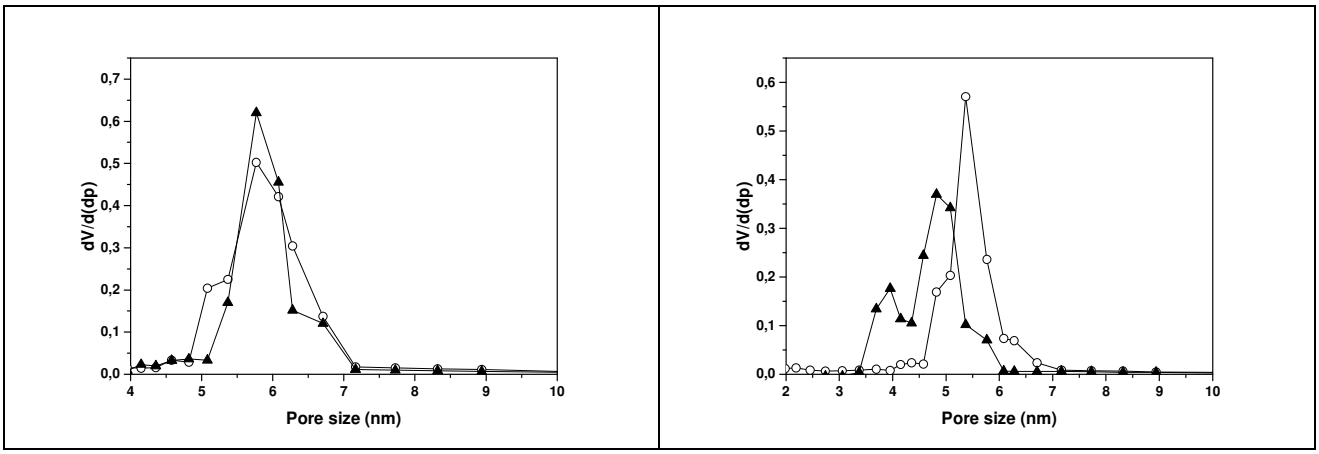

Figure 6. (Left) BJH pore size distribution of SBA-15-80 soaked into water (open circle) and OCP(CAN) 93 mg/g immobilized on SBA-15-80 under blue light (full triangle). (Right) BJH pore size distribution of SBA-15-80-NH_2 soaked into water (open circle) and OCP(CAN) 85 mg/g immobilized on SBA-15-80-NH_2 under blue light (full triangle).

Furthermore, photo-properties of OCP(ECN) and OCP(CAN) have been tested after protein immobilization on silica matrices, notably its photo-activation, to assess the influence of the surrounding environment on OCP photocycle, aiming to the development of nano-optical devices.

UV-Vis spectra of OCP(ECN) and OCP(CAN) solubilized in water are shown (Figure 7, I and II, respectively). In darkness, both protein solutions are orange colored. OCP(ECN) presents a vibrational structure with two maxima at 474 and 495 nm, while OCP(CAN) presents two maxima at 474 and 500 nm. Absorption of blue-green light converts, with a low yield [5], the orange form (OCP^O) to a metastable red form OCP^R whose spectrum loses the vibrational band resolution observed for OCP^O, undergoes an intensity decrease with a broader spectral shape and exhibits a redshift with a unique maximum at 511 nm for both OCP(CAN) and OCP(ECN).

The spectra of the echinenone and canthaxanthin alone in water have a similar shape to the one of OCP. In a polar solvent, the maximum of the electronic transition occurs at 476 nm for echinenone and 490 nm canthaxanthin [57,58]. The red shift observed between absorbance maximum of echinenone and canthaxanthin is related to the increasing number of conjugated double bounds (involving two carbonyl groups in canthaxanthin and one carbonyl group in echinenone). However, the absorbance behavior in the visible range allows to unambiguously decipher between OCP-bond carotenoid and carotenoid alone.

Suspensions of SBA-15 with immobilized OCP(CAN) and OCP(ECN) have been analyzed by UV-Vis spectroscopy before and after photo-activation with a blue light LED (Figure 7). In case of OCP(ECN), the UV-visible spectra recorded in the dark of SBA-15-80 after protein adsorption are similar to the ones recorded for $OCP(ECN)^O$ in solution (Figure 7I), with two local maxima at 474 et 495 nm (Figure 7, IA to 1D). It is thus likely that the immobilization process has no influence on the conformation of the OCP(ECN). However, photosensitivity of OCP(ECN) clearly differs be-

tween SBA-15-80 and SBA-15-120. While OCP(ECN) remains photoactive on SBA-15-80 with a unique local maximum observed at 508 nm, no significant shift of the maximum was observed after illumination for OCP(ECN) immobilized on SBA-15-120 (Figure 7. IA, IB). The properties of OCP(ECN) were however completely different when immobilized on functionalized SBA-15-NH_2 (Figure 7. IC, ID). Indeed, OCP(ECN) retains its orange form after immobilization and was able to shift to its red form after photoactivation: a unique local maximum was observed at 508 nm on SBA-15-80-NH_2 and 507 nm on SBA-15-120-NH_2, very close to the maximum observed for OCP^R in solution. OCP(ECN) thus remained photoactive when immobilized on SBA-15-NH_2, whatever the pore size.

In case of OCP(CAN) immobilized on native SBA-15, the UV-visible spectra recorded in the dark are very similar to the ones of the OCP^R form of the protein in solution whatever the pore size of the mesoporous silica (Figure 7. IIA, IIB). After photoactivation, no significant modification of the spectra was observed. It can therefore be concluded that OCP(CAN) was immobilized under its red form and consequently is inactive towards illumination when immobilized. Again, the properties of OCP(CAN) were however completely different when immobilized on functionalized SBA-15-NH_2 (Figure 7. IIC, IID). In the letter case, it was observed that OCP(CAN) retains its orange form after immobilization and that it was able to shift to its red form after photoactivation: a unique local maximum was observed at 508 nm on SBA-15-80-NH_2 and 510 nm on SBA-15-120-NH_2, very close to the maximum observed for OCP^R in solution.

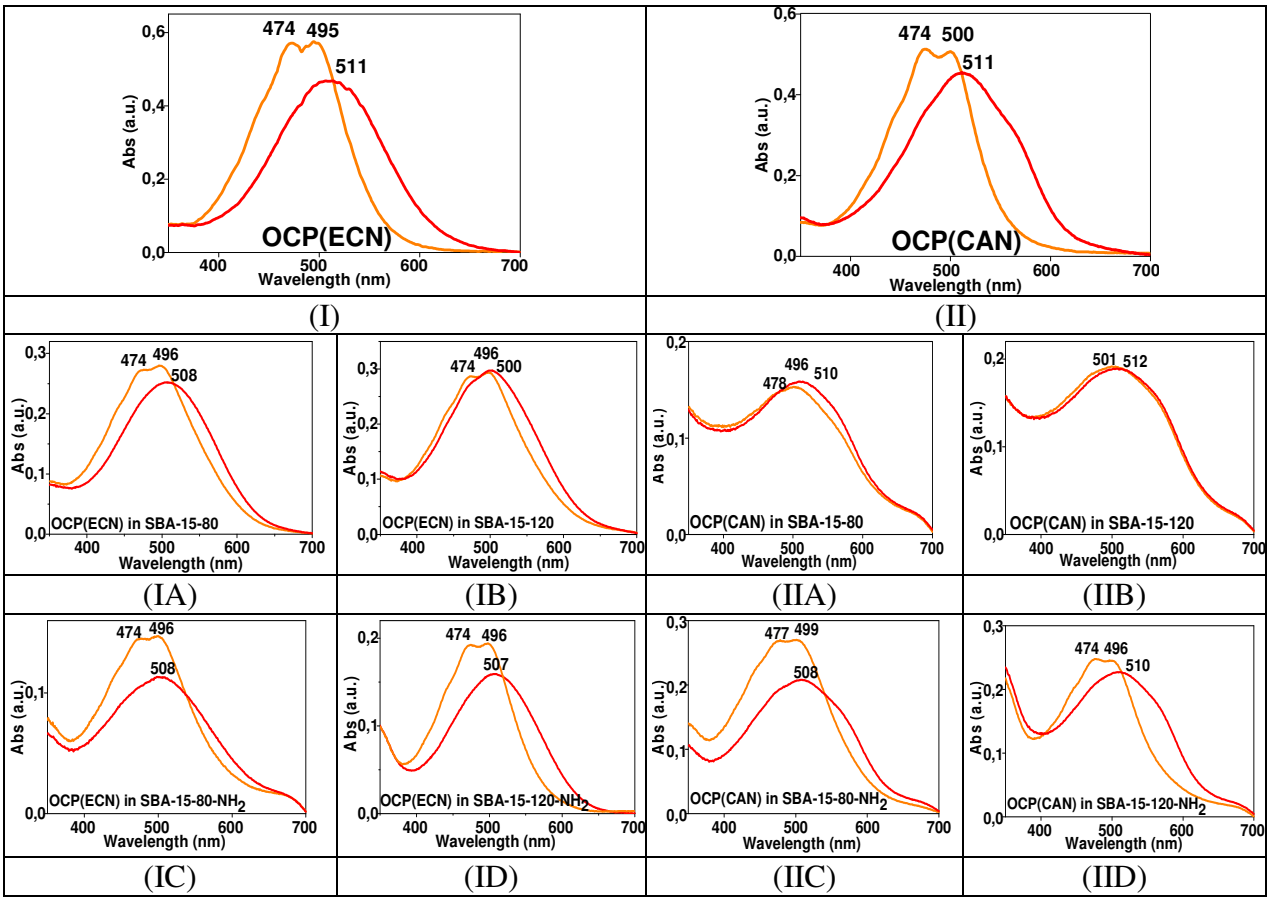

Figure 7. Visible spectra recorded in 350-700 nm range. Spectra before (orange) and after photoactivation with blue light LED (red). (I) OCP(ECN) in solution; (II) OCP(CAN) in solution. OCP(ECN) in SBA-15-80 (IA), SBA-15-120 (IB), SBA-15-80-NH_2 (IC), SBA-15-120-NH_2 (ID). OCP(CAN) in SBA-15-80 (IIA), SBA-15-120 (IIB), SBA-15-80-NH_2 (IIC), SBA-15-120-NH_2 (IID).

OCP(CAN) immobilized on SBA-15-120-NH_2 has been used to study the back-conversion of the protein on silica solid support and to compare it with the fast back-conversion occurring in solution. The sample, placed on UV-Vis solid phase sample holder, has been photo-activated with Blue light LED for 30 minutes. Then, spectra have been collected at different time intervals from time 0 up to 2h (Figure 8). Gradual back-conversion $OCP^R \rightarrow OCP^O$ was observed, with a slower different kinetic compared to the faster one occurring in solution (few seconds), likely attributable to the presence of matrix constrain. No back-conversion has been recorded for OCP(ECN) in any type of SBA-15. As a conclusion, the external constraint of SBA-15-NH_2 results in a slower back-conversion kinetic of OCP(CAN) after photoactivation.

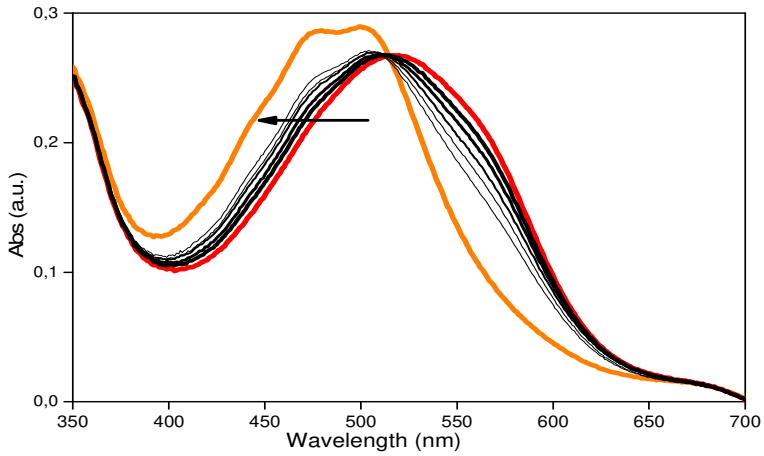

Figure 8. Visible spectra of OCP(CAN) in SBA-15-120-NH_2 following the photo-activation and relaxation of the protein. Before (orange), after blue light LED exposition (red), relaxation after 10, 20, 40, 60, 120 min in the dark (black lines from the thickest to the thinner following the arrow).

Stability of OCP(CAN) in solution and immobilized on SBA-15-80-NH_2 has been assessed. Samples have been stored at room temperature for 1 month in the dark and analyzed with UV-Vis spectroscopy in liquid and solid phase, before and after photoactivation with Blue light LED after one week and after one-month storage (Figure 9). After 1 week at RT in the dark, OCP(CAN) spectra in solution and immobilized on SBA-15-80-NH_2 are representative of the one of their orange conformations in solution. In addition, the protein converted into the red form in both cases, showing it keeps its photoactivation properties. After one-month storage at RT in the dark, OCP(CAN) in solution undergoes a partial conversion to the red form as demonstrated by the slight redshift of the spectrum and by the decrease of spectral intensity at 474 nm (Figure 9, left); despite this, the protein is still completely photoactive. On the contrary, when immobilized, OCP(CAN) is not photoactive. Indeed, before or after blue light exposition, spectral properties do not change: its spectrum blue-shifts and loses its vibrational structure, suggesting a modification of the interactions between canthaxanthin and its binding pocket.

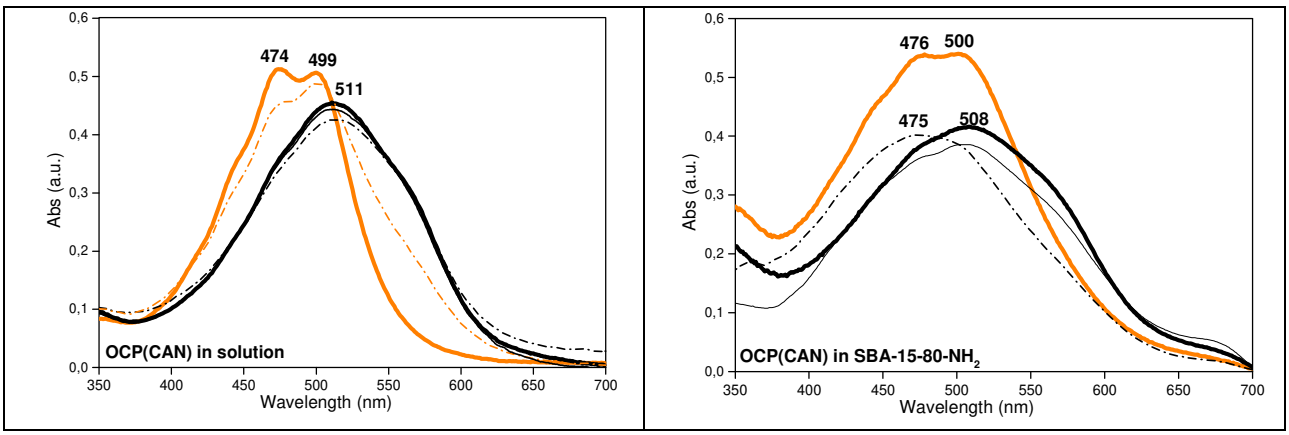

Figure 9. (Left) Vis spectra of OCP(CAN) 0.4 mg/mL in solution, before (orange) and after (thick black) exposition to blue light LED at t=0 (day of immobilization); after blue light LED at t=1week (thin black); before and after blue light LED at t=1 month (thin dash-dot-dash orange and black, respectively). (Right) Vis spectra of OCP(CAN) in SBA-15-80-NH_2, before (orange) and after (thick black) exposition to blue light LED at t=0; after blue light LED at t=1week (thin black); before and after blue light LED at t=1 month (thin dash-dot-dash black).

To summarize the results presented in this paragraph, the tested SBA-15 materials are suitable supports for the immobilization of both OCP(ECN) and OCP(CAN) by adsorption. With an initial OCP concentration in solution of 2 mg/mL, the protein loading in the dark reached 52 mg/g on native SBA-15-80 while an 18 mg/g maximal loading was measured on the corresponding functionalized mesoporous material with aminopropyl groups. The immobilization yield could be significantly enhanced when the immobilization experiments were performed in the presence of light for both bare and functionalized materials, which was interpreted as a clue of the OCP(CAN) uptake into the meso-porosity of silica, in addition to the observed decrease of the mesopores diameter of SBA-15-80-NH_2 after protein loading. To our knowledge, this is the first report on successful use of a photoactivation process to enhance protein immobilization. In addition, experimental evidence showed that both OCP(ECN) and OCP(CAN) remain photoactive when immobilized on organo-functionalized SBA-15-NH_2 whatever the pore size of the functionalized material, allowing to consider the use of immobilized OCP for applications involving a photoactivation process.

3.3 OCP leaching extent from SBA-15-80 or SBA-15-80-NH_2

The release of OCP(CAN) adsorbed on SBA-15-80 or SBA-15-80-NH_2 (quantity of adsorbed OCP 38 and 33 mg/g of solid, respectively) was assayed in different conditions. Adsorption of OCP is likely to be driven by electrostatic interactions between the support and the protein. At pH around 7, SBA-15-80 surface is negatively charged due to the deprotonation of free silanol groups while it is positively charged for SBA-15-80-NH_2 due to the grafting of aminopropyl groups. This was confirmed by zeta potential measurements (see SI). On the other hand, OCP is overall negatively charged at pH 7 since its isoelectric point is around 5.4, as calculated from its primary sequence. Consequently, electrostatic interactions OCP and SBA-15-80-NH_2 are favoured at pH 7. The opposite is observed concerning OCP and SBA-15-80. To screen the positive interactions with SBA-15-NH_2 and favour OCP desorption, the ionic strength of the solution was increased with NaCl 1M. Up to 12.5 % of OCP leaching from SBA-15-80-NH_2 was observed after 24 hours. Surprisingly, the leaching extent decreased after one week. Lower leaching (around 2 %) was observed from SBA-15-80. These results, together with the fact that very similar amounts of OCP could be adsorbed on SBA-15-80 and SBA-15-80-NH_2 at pH 8.5 while electrostatic interactions between OCP and the support are opposite, could corroborate the hypothesis that electrostatic interactions are not the main driving force of OCP adsorption. To help to clarify this point, leaching of OCP from SBA-15-80-

NH_2 was assessed in unfavourable electrostatic conditions, i.e., at pH 4.2 where OCP overall charge and the surface charge are both positive. In such conditions, the OCP leaching reached 18.5 % after 24 hours and 7 % after one week. Such conditions are thus more efficient, which is compatible with a contribution of electrostatic forces in the OCP adsorption process. In anyway light-induced leaching was tested but no effect has been detected suggesting that photo-conversion of OCP and its structural rearrangement do not help the release of the protein.

OCP (CAN) leaching extent (%)	**NaCl 1 M**		**pH**		
	24h	**1 week**		**24h**	**1 week**
SBA-15-80	2.5 %	2 %	7.3	2 %	2 %
SBA-15-80-NH_2	12.5 %	5 %	4.2	18.5 %	7 %

Table 3. Leaching extent of OCP(CAN) from SBA-15-80 and SBA-15-80-NH_2 in NaCl 1 M or pH effect (pH 7.3 for SBA-15-80 and pH 4.3 for SBA-15-80NH_2).

Interestingly, the leaching extent of OCP(CAN) from SBA-15-80 could be discussed in relationship with the photoactivity of immobilized OCP, which was irreversibly converted to its red form after its adsorption. Together with the very low leaching observed, it could be concluded that its adsorption induces an irreversible conformational change into the red form of the protein (and an irreversible adsorption), probably related to strong interactions between specific moieties of the red form of the protein and silanol groups. On the contrary, the preserved photoactivity of OCP(CAN) on SBA-15-80-NH_2 is somehow consistent with a partly reversible adsorption of the protein.

4. Conclusions

In conclusion, considering the wide range of nanobiotechnological applications involving the immobilization of proteins, this work has achieved several goals. 1) SBA-15 meso-porous materials synthesized at different aging temperature, bare and organo-functionalized, have shown a worm shape morphology with well-ordered crystalline structure which is not affected by the functionalization with amino groups. 2) SBA-15 materials with two different pore sizes are suitable and promising supports for the immobilization of both OCP(ECN) and OCP(CAN) by adsorption. The equilibrium of immobilization, driven by electrostatic interactions, is reached after 4 hours on both types of SBA-15, bare and organo-functionalized, and the maximum loading yield is achieved for an initial OCP concentration of 0.2 mg/mL. At higher initial OCP concentration, the amount of immobilized OCP was enhanced up to more than 30 mg of protein per g of material. 3) Illumination by blue light increases immobilization efficiency on both SBA-15-80 and SBA-15-80-NH_2 nanoparticles, leading to around four-fold more immobilized OCP and suggesting that the conformation of OCP (ellipsoidal for OCP^O and more elongated for OCP^R) plays a key-role in entering the mesopores thereby increasing protein loading. 4) Protein photo-activity is completely preserved after immobilization on SBA-15-NH_2 if compared with SBA-15 which, on the contrary, tends to dark-activate the protein converting it into OCP^R, except in case of OCP(ECN) which remained photoactive on SBA-15-80. 5) OCP@SBA-15-NH_2 looks a promising photo-active system, still stable after 1 week

at room temperature, able to slow down the kinetic of back conversion $OCP^R \rightarrow OCP^O$. This property can, in principle, be exploited in several domains: from biocompatible photochromic nanoparticles to the development of nano-scaled supports for caroteno-proteins and carotenoid delivery and release. In the latter case, further studies should be undertaken in order to improve the release extend of OCP, for example by varying the functionalized groups grafted on the solid, thus modulating the interactions between the protein and the surface.

Funding: This research and the APC was funded by French state funds within the framework of the doctoral school "Physique et chimie des matériaux" (ED 397) held by Sorbonne Université. This work was partially supported by the grant obtained from the Agence Nationale de la Recherche (DynOCP [ANR-18-CE11-0005-03]. This research was also supported by the Centre National de la Recherche Scientifique (CNRS) and the Commissariat à l'Energie Atomique et énergies alternatives (CEA). S. Leccese was partially funded by Università degli Studi di Bari – A. Moro through a predoctoral financial support.

References

[1] L.C. Sang, A. Vinu, M.O. Coppens, Langmuir. 27 (2011) 13828–13837. https://doi.org/10.1021/la202907f.
[2] P.R.A.F. Garcia, R.N. Bicev, C.L.P. Oliveira, O.A. Sant'Anna, M.C.A. Fantini, Microporous Mesoporous Mater. 235 (2016) 59–68. https://doi.org/10.1016/j.micromeso.2016.07.033.
[3] J. Siefker, R. Biehl, M. Kruteva, A. Feoktystov, M.O. Coppens, J. Am. Chem. Soc. 140 (2018) 12720–12723. https://doi.org/10.1021/jacs.8b08454.
[4] M. Hartmann, Chem. Mater. 17 (2005) 4577–4593. https://doi.org/10.1021/cm0485658.
[5] F. Muzzopappa, D. Kirilovsky, Trends Plant Sci. 25 (2020) 92–104. https://doi.org/10.1016/j.tplants.2019.09.013.
[6] D. Kirilovsky, C.A. Kerfeld, Nat. Plants. 2 (2016) 16180. https://doi.org/10.1038/nplants.2016.180.
[7] A. Wilson, J.N. Kinney, P.H. Zwart, C. Punginelli, S. D'Haene, F. Perreau, M.G. Klein, D. Kirilovsky, C.A. Kerfeld, J. Biol. Chem. 285 (2010) 18364–18375. https://doi.org/10.1074/jbc.M110.115709.
[8] R.L. Leverenz, M. Sutter, A. Wilson, S. Gupta, A. Thurotte, C.B. De Carbon, C.J. Petzold, C. Ralston, F. Perreau, D. Kirilovsky, C.A. Kerfeld, Science (80-.). 348 (2015) 1463–1466. https://doi.org/10.1126/science.aaa7234.
[9] I. Domonkos, M. Kis, Z. Gombos, B. Ughy, Prog. Lipid Res. 52 (2013) 539–561. https://doi.org/10.1016/j.plipres.2013.07.001.
[10] A. Pérez-gálvez, I. Viera, M. Roca, Antioxidants. 9 (2020) 1–39. https://doi.org/10.3390/antiox9060505.
[11] E. Fernández-García, I. Carvajal-Lérida, M. Jarén-Galán, J. Garrido-Fernández, A. Pérez-Gálvez, D. Hornero-Méndez, Food Res. Int. 46 (2012) 438–450. https://doi.org/10.1016/j.foodres.2011.06.007.
[12] A. V. Rao, L.G. Rao, Pharmacol. Res. 55 (2007) 207–216. https://doi.org/10.1016/j.phrs.2007.01.012.
[13] E.G. Maksimov, A. V Zamaraev, E.Y. Parshina, Y.B. Slonimskiy, T.A. Slastnikova, A.A. Abdrakhmanov, P.A. Babaev, S.S. Efimova, O.S. Ostroumova, A. V Stepanov, E.A. Slutskaya, A. V Ryabova, T. Friedrich, N.N. Sluchanko, M.M. Shemyakin, Y.A. Ovchinnikov, A.M. Prokhorov, Antioxidants. 2020 (n.d.) 869. https://doi.org/10.3390/antiox9090869.

[14] A. Andreoni, S. Lin, H. Liu, R.E. Blankenship, H. Yan, N.W. Woodbury, Nano Lett. 17 (2017) 1174–1180. https://doi.org/10.1021/acs.nanolett.6b04846.
[15] E.G. Maksimov, W.J. Li, E.A. Protasova, T. Friedrich, B. Ge, S. Qin, N.N. Sluchanko, Biochem. Biophys. Res. Commun. 516 (2019) 699–704. https://doi.org/10.1016/j.bbrc.2019.06.098.
[16] E.G. Maksimov, I.A. Yaroshevich, G. V. Tsoraev, N.N. Sluchanko, E.A. Slutskaya, O.G. Shamborant, T. V. Bobik, T. Friedrich, A. V. Stepanov, Sci. Rep. 9 (2019) 1–9. https://doi.org/10.1038/s41598-019-45421-7.
[17] F. Muzzopappa, A. Wilson, D. Kirilovsky, Nat. Plants. 5 (2019) 1076–1086. https://doi.org/10.1038/s41477-019-0514-9.
[18] M.A. Dominguez-Martin, C.A. Kerfeld, Curr. Opin. Struct. Biol. 57 (2019) 110–117. https://doi.org/10.1016/j.sbi.2019.01.023.
[19] Y.B. Slonimskiy, E.G. Maksimov, E.P. Lukashev, M. Moldenhauer, T. Friedrich, N.N. Sluchanko, Biochim. Biophys. Acta - Bioenerg. 1861 (2020) 148174. https://doi.org/10.1016/j.bbabio.2020.148174.
[20] M. Moldenhauer, N.N. Sluchanko, D. Buhrke, D. V. Zlenko, N.N. Tavraz, F.J. Schmitt, P. Hildebrandt, E.G. Maksimov, T. Friedrich, Photosynth. Res. 133 (2017) 327–341. https://doi.org/10.1007/s11120-017-0353-3.
[21] M. Hartmann, X. Kostrov, Chem. Soc. Rev. 42 (2013) 6277–6289. https://doi.org/10.1039/c3cs60021a.
[22] D. Zhao, J. Feng, Q. Huo, N. Melosh, G.H. Fredrickson, B.F. Chmelka, G.D. Stucky, Science (80-.). 279 (1998) 548–552. https://doi.org/10.1126/science.279.5350.548.
[23] Ł. Laskowski, M. Laskowska, N. Vila, M. Schabikowski, A. Walcarius, Molecules. 24 (2019) 1–31. https://doi.org/10.3390/molecules24132395.
[24] M. Imperor-Clerc, P. Davidson, A. Davidson, J. Am. Chem. Soc. 122 (2000) 11925–11933. https://doi.org/10.1021/ja002245h.
[25] F. Sevimli, A. Yilmaz, Microporous Mesoporous Mater. 158 (2012) 281–291. https://doi.org/10.1016/j.micromeso.2012.02.037.
[26] M. Martínez-Carmona, A. Baeza, M.A. Rodriguez-Milla, J. García-Castro, M. Vallet-Regí, J. Mater. Chem. B. 3 (2015) 5746–5752. https://doi.org/10.1039/c5tb00304k.
[27] E. Ahmadi, N. Dehghannejad, S. Hashemikia, M. Ghasemnejad, H. Tabebordbar, Drug Deliv. 21 (2014) 164–172. https://doi.org/10.3109/10717544.2013.838715.
[28] K. Scaramuzzi, G.D. Tanaka, F.M. Neto, P.R.A.F. Garcia, J.J.M. Gabrili, D.C.A. Oliveira, D. V. Tambourgi, J.S. Mussalem, D. Paixão-Cavalcante, M.T. D'Azeredo Orlando, V.F. Botosso, C.L.P. Oliveira, M.C.A. Fantini, O.A. Sant'Anna, Nanomedicine Nanotechnology, Biol. Med. 12 (2016) 2241–2250. https://doi.org/10.1016/j.nano.2016.06.003.
[29] C.B. De Carbon, A. Thurotte, A. Wilson, F. Perreau, D. Kirilovsky, Sci. Rep. 5 (2015) 1–8. https://doi.org/10.1038/srep09085.
[30] A. Vinu, C. Streb, V. Murugesan, M. Hartmann, J. Phys. Chem. B. 107 (2003) 8297–8299. https://doi.org/10.1021/jp035246f.
[31] A. Galarneau, H. Cambon, F. Di Renzo, F. Fajula, Langmuir. 17 (2001) 8328–8335. https://doi.org/10.1021/la0105477.
[32] A. Galarneau, H. Ne Cambon, F. Di Renzo, R. Ryoo, M. Choi, F. Fajula, New J. Chem., 27 (2003) 73-79. https://doi.org/10.1039/b207378c.
[33] A.B. Fuertes, Microporous Mesoporous Mater. 67 (2004) 273–281. https://doi.org/10.1016/j.micromeso.2003.11.012.
[34] T. Benamor, L. Vidal, B. Lebeau, C. Marichal, Microporous Mesoporous Mater. 153 (2012) 100–114. https://doi.org/10.1016/j.micromeso.2011.12.016.
[35] S.M.L. Santos, J.A. Cecilia, E. Vilarrasa-García, I.J. Silva Junior, E. Rodríguez-Castellón, D.C.S. Azevedo, Microporous Mesoporous Mater. 232 (2016) 53–64. https://doi.org/10.1016/j.micromeso.2016.06.004.
[36] A. Katiyar, S. Yadav, P.G. Smirniotis, N.G. Pinto, J. Chromatogr. A. 1122 (2006) 13–20.

https://doi.org/10.1016/j.chroma.2006.04.055.
[37] D. Jung, C. Streb, M. Hartmann, Microporous Mesoporous Mater. 113 (2008) 523–529. https://doi.org/10.1016/j.micromeso.2007.12.009.
[38] N.H. Abdallah, M. Schlumpberger, D.A. Gaffney, J.P. Hanrahan, J.M. Tobin, E. Magner, J. Mol. Catal. B Enzym. 108 (2014) 82–88. https://doi.org/10.1016/j.molcatb.2014.06.007.
[39] Q. Tao, Z. Xu, J. Wang, F. Liu, H. Wan, S. Zheng, Microporous Mesoporous Mater. 131 (2010) 177–185. https://doi.org/10.1016/j.micromeso.2009.12.018.
[40] J. Meissner, A. Prause, C. Di Tommaso, B. Bharti, G.H. Findenegg, J. Phys. Chem. C. 119 (2015) 2438–2446. https://doi.org/10.1021/jp5096745.
[41] A.S. Maria Chong, X.S. Zhao, J. Phys. Chem. B. 107 (2003) 12650–12657. https://doi.org/10.1021/jp035877+.
[42] N. Balistreri, D. Gaboriau, C. Jolivalt, F. Launay, J. Mol. Catal. B Enzym. 127 (2016) 26–33. https://doi.org/10.1016/j.molcatb.2016.02.003.
[43] D. Jung, C. Streb, M. Hartmann, Int. J. Mol. Sci. 11 (2010) 762–778. https://doi.org/10.3390/ijms11020762.
[44] B.-H. Min, E.-Y. Jeong, M. Thommes, S.-E. Park, Chem. Commun. 47 (2011) 4673–4675. https://doi.org/10.1039/c1cc10420a.
[45] K.C. Kao, T.S. Lin, C.Y. Mou, J. Phys. Chem. C. 118 (2014) 6734–6743. https://doi.org/10.1021/jp4112684.
[46] J. Kijima, Y. Shibuya, K. Katayama, T. Itoh, H. Iwase, Y. Fukushima, M. Kubo, A. Yamaguchi, J. Phys. Chem. C. 122 (2018) 15567–15574. https://doi.org/10.1021/acs.jpcc.8b04356.
[47] L.C. Sang, A. Vinu, M.O. Coppens, Langmuir. 27 (2011) 13828–13837. https://doi.org/10.1021/la202907f.
[48] J. Meissner, A. Prause, B. Bharti, G.H. Findenegg, Colloid Polym. Sci. 293 (2015) 3381–3391. https://doi.org/10.1007/s00396-015-3754-x.
[49] Z. Wu, D. Zhao, Chem. Commun. 47 (2011) 3332–3338. https://doi.org/10.1039/c0cc04909c.
[50] E.G. Maksimov, N.N. Sluchanko, Y.B. Slonimskiy, E.A. Slutskaya, A. V. Stepanov, A.M. Argentova-Stevens, E.A. Shirshin, G. V. Tsoraev, K.E. Klementiev, O. V. Slatinskaya, E.P. Lukashev, T. Friedrich, V.Z. Paschenko, A.B. Rubin, Sci. Rep. 7 (2017) 1–12. https://doi.org/10.1038/s41598-017-15520-4.
[51] Y.B. Slonimskiy, F. Muzzopappa, E.G. Maksimov, A. Wilson, T. Friedrich, D. Kirilovsky, N.N. Sluchanko, FEBS J. 286 (2019) 1908–1924. https://doi.org/10.1111/febs.14803.
[52] M. Gwizdala, A. Wilson, D. Kirilovsky, Plant Cell. 23 (2011) 2631–2643. https://doi.org/10.1105/tpc.111.086884.
[53] S. Gupta, M. Guttman, R.L. Leverenz, K. Zhumadilova, E.G. Pawlowski, C.J. Petzold, K.K. Lee, C.Y. Ralston, C.A. Kerfeld, Proc. Natl. Acad. Sci. U. S. A. 112 (2015) E5567–E5574. https://doi.org/10.1073/pnas.1512240112.
[54] E.G. Maksimov, N.N. Sluchanko, Y.B. Slonimskiy, K.S. Mironov, K.E. Klementiev, M. Moldenhauer, T. Friedrich, D.A. Los, V.Z. Paschenko, A.B. Rubin, Biophys. J. 113 (2017) 402–414. https://doi.org/10.1016/j.bpj.2017.06.002.
[55] S. Bandara, Z. Ren, L. Lu, X. Zeng, H. Shin, K.H. Zhao, X. Yang, Proc. Natl. Acad. Sci. U. S. A. 114 (2017) 6286–6291. https://doi.org/10.1073/pnas.1700956114.
[56] M. Golub, M. Moldenhauer, F.J. Schmitt, W. Lohstroh, E.G. Maksimov, T. Friedrich, J. Pieper, J. Phys. Chem. B. 123 (2019) 9536–9545. https://doi.org/10.1021/acs.jpcb.9b05073.
[57] P. Chábera, M. Fuciman, P. Híbek, T. Polívka, Phys. Chem. Chem. Phys. 11 (2009) 8795–8803. https://doi.org/10.1039/b909924g.
[58] B. Fernández-González, G. Sandmann, A. Vioque, J. Biol. Chem. 272 (1997) 9728–9733. https://doi.org/10.1074/jbc.272.15.9728.

Graphical abstract